Accepted Manuscript

Title: Hydrothermal synthesis of reduced graphene oxide-$CoFe_2O_4$ heteroarchitecture for high visible light photocatalytic activity: Exploration of efficiency, stability and mechanistic pathways

Authors: L. Gomathi Devi, M. Srinivas

PII: S2213-3437(17)30273-7
DOI: http://dx.doi.org/doi:10.1016/j.jece.2017.06.023
Reference: JECE 1685

To appear in:

Received date: 6-3-2017
Revised date: 9-6-2017
Accepted date: 13-6-2017

Please cite this article as: L.Gomathi Devi, M.Srinivas, Hydrothermal synthesis of reduced graphene oxide-CoFe2O4 heteroarchitecture for high visible light photocatalytic activity: Exploration of efficiency, stability and mechanistic pathways, Journal of Environmental Chemical Engineeringhttp://dx.doi.org/10.1016/j.jece.2017.06.023

Hydrothermal synthesis of Reduced Graphene Oxide-$CoFe_2O_4$ heteroarchitecture for high visible light photocatalytic activity: Exploration of efficiency, stability and mechanistic pathways

L. Gomathi Devi*, Srinivas. M

Department of Post Graduate Studies in Chemistry, Central College City Campus,

Dr. Ambedkar Street, Bangalore University, Bangalore-560001, INDIA

E-mail: gomatidevi_naik@yahoo.co.in

Graphical abstract

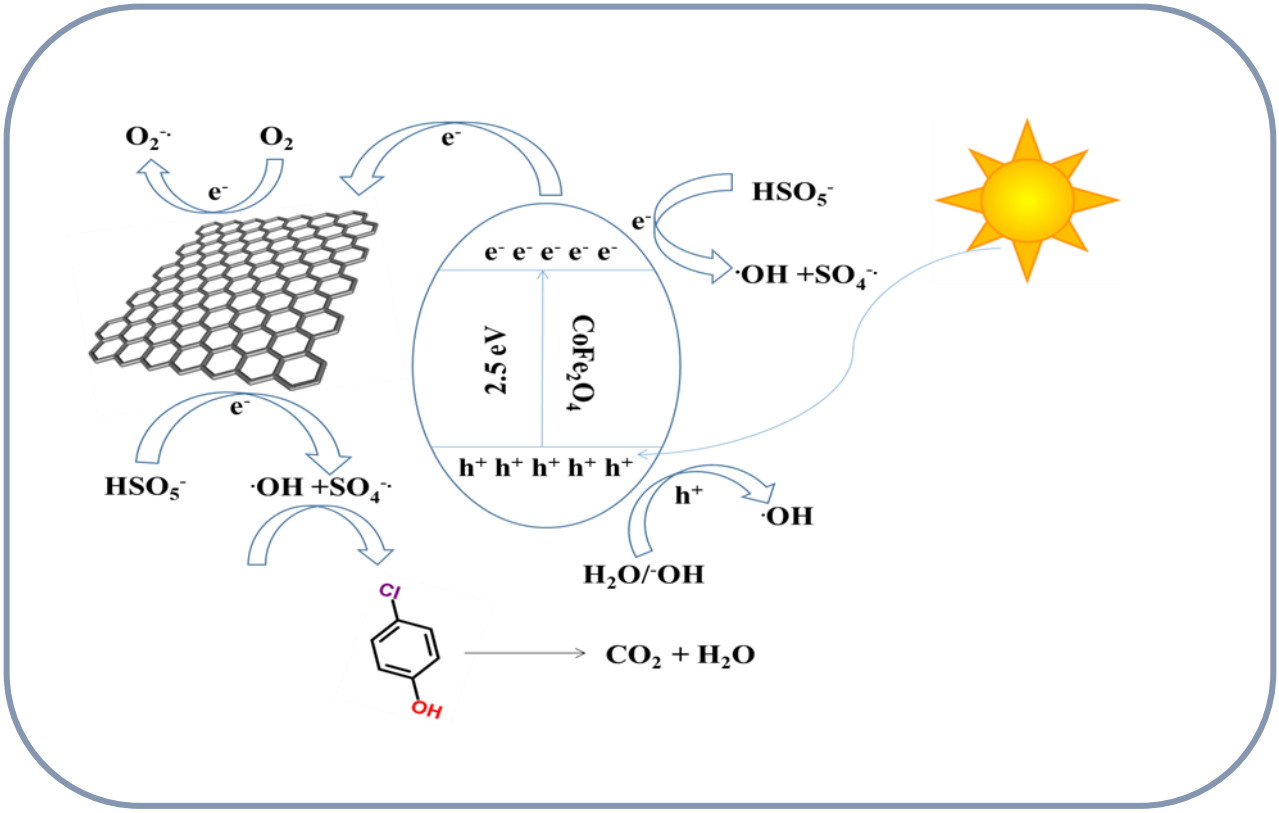

Photocatalytic process involving RGO-$CoFe_2O_4$ heterostructure transformation of the structure from normal spinel to inverse spinel and vice versa may continuously take place via the electron trapping and detrapping by Fe^{3+} and Co^{2+} ions.

Abstract

RGO-$CoFe_2O_4$ heterostructure nanocomposite was prepared by hydrothermal method and was characterized by various analytical techniques such as Powder X-ray Diffraction method (PXRD), UV-visible absorbance, Photoluminescence (PL), Fourier Transform Infra Red (FTIR) spectroscopic techniques, BET surface area measurements, Field Emission Scanning Electron Microscopy (FESEM), Raman Spectroscopy and Vibrating Sample Magnetometer (VSM). The results confirmed the formation of hybrid structure with $CoFe_2O_4$ particles embedded in RGO sheets. Photocatalytic activity of the nanocomposites was probed for the degradation of 4-Chlorophenol (4-CP) as the model compound under the visible light illumination. The photocatalytic activity decreases in the following order RGO-$CoFe_2O_4$ >$CoFe_2O_4$ >RGO. Further the activity of RGO-$CoFe_2O_4$ composite was explored in the presence of peroxymonosulfate (PMS) as an oxidant. LUMO of PMS can accommodate photogenerated electrons, thereby suppresses the recombination process. The enhanced activity of RGO-$CoFe_2O_4$ hybrid is compared to its individual counterparts and the higher activity is accounted to its unique electronic structure. RGO serves as electron acceptor from $CoFe_2O_4$ and electron donor to the oxygen molecule. During the photocatalysis, transformation of the native structure from normal spinel to inverse spinel and vice versa may take place continuously from the process of electron trapping and detrapping by Fe^{3+} and Co^{2+}ions. The observed continuous absorption for RGO-$CoFe_2O_4$ composite in the UV-visible spectra implies active d-d transitions involving transition metals present in the nanocomposite.

Keywords: $CoFe_2O_4$, Normal spinel, Inverse spinel, Reduced graphene oxide, Peroxymonosulfate.

1. INTRODUCTION

It is of great interest to explore new materials with multifunctional properties for energy and environment applications. Many of the wide band gap semiconductor materials tested so far are found to be active only under UV light and these materials are proven to be stable in aqueous medium [1-8]. Thus under the best circumstances they absorb less than 10% of the incident solar radiant energy. There are several other metal oxide materials with smaller band gap like Fe_2O_3, Co_3O_4, V_2O_5 etc., which are good sunlight absorbers but their conduction band is located at considerably lower energy (0.5 eV) than the position of hydrogen redox potential level. In such cases the photogenerated electrons are unable to reduce H_2O into H_2 without the aid of external bias. Therefore, it appears that a good way to tackle these problems might be to alter the properties of the materials which are already giving best response and to improve their efficiencies [9-13]. Spinel ferrite material with narrow band gap and which can absorb natural sunlight draws the attention of many researchers. Previous studies have shown the enhanced photocatalytic activities for some of the ferrite nanoparticles [14-17]. Literature shows that RGO imparts longer life for the photogenerated charge carriers by providing channels for the movement of electrons [18-29]. He et. al., have used $CoFe_2O_4$ nanoparticles and RGO-$CoFe_2O_4$ hybrid nanostructures for the degradation of malachite green in the water by both photocatalysis and photo-Fenton process. They show a remarkable increase in the rate with increase in the H_2O_2 concentration [31]. Chen et. al., have prepared RGO-$CoFe_2O_4$ composite by ball milling process and reports its efficiency for the degradation of methylene blue, rhodomine B and methyl orange under visible light irradiation [32]. Ghosh et. al., have synthesized RGO-$CoFe_2O_4$ catalyst by in situ co-precipitation reduction method and the catalyst is shown to have excellent microwave absorbing property as well as high photocatalytic activity under visible light [33]. Cao et. al., have prepared RGO-$CoFe_2O_4$ by solvothermal method. Their synthesis process includes conversion of graphite to graphene oxide by Hammers method followed by the process of

incorporation of Fe^{3+} and Co^{2+}ions by ion exchange method. Further the product was subjected to solvothermal process in the presence of $N_2H_4.H_2O$. They have reported good adsorption performance for their prepared catalyst [34]. Pu et. al., have prepared RGO-$CoFe_2O_4$ by combustion method and the higher performance of their catalyst is attributed to the efficient transfer of photogenerated electrons from $CoFe_2O_4$ to graphene sheets [35]. $CoFe_2O_4$ is a mixed metal oxide having spinel structure with Fe^{3+} ions in the octahedral sites. The spinels have general formula AB_2O_4 where, A can be group IIA metal ion or a transition metal ion in +2 oxidation state and B can be a group IIIA metal ion or a transition metal ion in +3 oxidation state. The oxide ions form close packed cubic lattice with 8 tetrahedral holes and 4 octahedral holes per AB_2O_4 unit. Although, pure $CoFe_2O_4$ itself is photocatalytically active under visible light irradiation, it is further possible to improve the photocatalytic efficiency by coupling it with Reduced Graphene Oxide (RGO). RGO coupled with $CoFe_2O_4$ composite is expected to show excellent performance both under UV and visible light. Such heterostructure systems show high specificity in the reaction mechanism in addition to its higher performance under the visible light irradiation. In the present research $CoFe_2O_4$ and RGO-$CoFe_2O_4$ composite were prepared by simple one step hydrothermal method. Further an attempt is made to provide a new physical insight on the charge carrier dynamics based on the electronic configuration of Co^{2+} and Fe^{3+} metal ions, especially the mechanism of charge carrier generation, trapping, interfacial charge transfer and recombination process. Although, the literature shows enhanced activity for RGO-$CoFe_2O_4$, we have shown that the activity of this material is a complex function of several physico-chemical and electronic properties. The individual contribution of each metal oxide in the composite to the overall efficiency is explored. It is promising multi-functional material for both environmental remediation and energy conversion. Its activity is further explored in the presence of Peroxymonosulphate (PMS), an electron acceptor commonly known as oxone.

2. EXPERIMENTAL SECTION

2.1. Materials

Graphene oxide, concentrated sulfuric acid (98%), peroxymonosulphate (PMS), hydrochloric acid, sodium hydroxide, absolute ethanol, $Fe(NO_3)_3.9H_2O$, $Co(NO_3)_2.6H_2O$ and 4-chlorophenol were of analytical grade reagents and they were provided by Sigma Aldrich. All the reagents were used without further purification. Double distilled water was used for all the experiments.

2.2. Method of preparation of catalysts.

Cobalt ferrite ($CoFe_2O_4$) was prepared by hydrothermal method. 0.0662 g of $Co(NO_3)_2.6H_2O$ and 0.1837 g of $Fe(NO_3)_3.9H_2O$ were dissolved in 20 mL of absolute ethanol by stirring the solution for 30 min. Further, the pH of the reaction solution was adjusted to 10 by using 6 M NaOH solution and the stirring of reaction mixture was continued for 30 min. The above reaction mixture was transferred to a teflon-lined autoclave and kept at 180^o C in a furnace for 6 h. The precipitate obtained from this hydrothermal method was filtered and washed with distilled water for several times and then finally with absolute ethanol. The precipitate was dried at 60^0 C in an oven to obtain $CoFe_2O_4$

Exfoliated graphene oxide (XGO) was prepared by taking 1.0 g of graphene oxide (GO) dispersed in 500 mL of distilled water and was subjected to ultrasonication for 2 hr. This suspension was further centrifuged for the removal of any unexfoliated GO. The residue was dried at 45^0 C for 24 h to obtain XGO.

Reduced graphene oxide (RGO) was synthesised by taking 0.4 g of XGO dispersed in 800 mL of distilled water by continues stirring and heating at 95^0 C for 12 hrs. The obtained RGO solid was dried at 60^o C.

RGO–$CoFe_2O_4$ composite was synthesized by hydrothermal method according to the method suggested by Fu et al., [36]. 0.3 g of RGO was dispersed in 60 mL of absolute ethanol and

was subjected to sonication for 1 h. As mentioned previously a solution was made by taking 0.0662 g of $Co(NO_3)_2.6H_2O$ and 0.1837 g of $Fe(NO_3)_3.9H_2O$ in 20 mL of absolute ethanol. The above two solutions were mixed together and stirred for 30 min. The pH of the solution was adjusted to 10 with 6 M NaOH solution and resulting mixture is further continuously stirred for 30 min, which yields a stable bottle-green homogeneous suspension. The resultant mixture was subjected to hydrothermal treatment by transferring it to a 100 mL teflon-lined stainless steel autoclave which was heated at 180^0 C for 20 h. Finally, the obtained precipitate was filtered, washed with distilled water several times and finally with absolute ethanol. This RGO–$CoFe_2O_4$ precipitate was dried in an oven at 60^0 C.

2.3. Characterization techniques

The crystal structures of RGO, $CoFe_2O_4$ and RGO-$CoFe_2O_4$ catalysts were investigated by using Bruker D8-Adavnace Powder X-ray diffractometer (PXRD) with Cu Kα (λ=1.541 Å) as source with accelerating voltage and current of 40 kV and 40 mA respectively. FTIR spectra were recorded on Perkin-Elmer spectrophotometer with a resolution of $4cm^{-1}$ in transition mode at room temperature using KBr pellets. The morphology of the materials were characterized by FESEM (Zeiss Neon 40EsB FIBSEM) equipped with EDS. The surface area, pore volume and pore size distribution of all the samples were determined by N_2 adsorption technique using Autosorb Quantachrome Corp Instrument at -196º C. All the samples were degassed at 100^0 C for 4 h prior to the adsorption experiments. The values of surface area, pore diameter and pore volume were obtained by using Brunauer-Emmett-Teller (BET) equation. The pore size distribution was obtained by the Barrett-Joyner-Halenda (BJH) method. Magnetic measurements were made using a Vibrating Sample Magnetometer (VSM) (Lake Shore 7410, Lake Shore Cryotronics, Inc., USA) at 25º C ± 2º C. Raman spectra of the samples were recorded at 633 nm laser excitation by using a DXR Raman Spectrophotometer (Thermo Fisher Scientific, USA). UV-visible absorbance spectra (UV-

Vis-DRS) were recorded in the wavelength range of 200 to 800 nm using a SPECORD 210 Plus spectrometer (Analytik Jena, Germany).

The photocurrent measurements were made under UV light irradiation using an electrochemical analyzer (CH Instruments) in a standard three-electrode system. The electrochemical cell consists of platinum electrodes as anode and cathode (having an active surface area of *ca*. 0.5 cm^2) in an electrolyte (0.1 M Na_2SO_4) suspension containing catalyst particles along with Ag/AgCl (saturated with KCl) reference electrode. 125 W medium pressure mercury vapour lamp was used as the UV light source. The photon flux of the UV light source was determined by ferrioxalate actinometry and was found to be 6.95 mW/cm^2. The emission wavelength was in the range of 350-400 nm with the λ_{max} around 370 nm. The irradiation was carried out by focusing the light directly into the reaction mixture in the open air condition at a distance of 29 cm.

2.4. Photochemical reactor

Experiments were carried out at room temperature using a circular glass reactor whose surface area is 176.6 cm^2. All the experiments were performed using double distilled water. Solar light experiments were performed under direct sunlight between 11 a.m. to 2 p.m. when the fluctuations in the solar light intensity was minimum. The experiments were conducted at Bangalore, India. The latitude and longitude are 12.58 N and 77.38 E respectively. The temperature of the reaction mixture was found to be around 28-30^0 C. The average solar intensity was found to be 0.753 kW/m^2 (using solar radiometer). The intensity of the solar light was concentrated by using a convex lens and the reaction mixture was directly exposed to this concentrated sunlight. The solar radiation as a function of wavelength was measured by photometer, which shows a maximum at 450 nm. To compare the photocatalytic activity of the catalysts, experiments were simultaneously conducted to minimize the error arising

due to the fluctuations in solar intensity. Further each experiment was repeated three times to find the consecutive values. Typical experiment contains 0.1 g of photocatalyst s(RGO/$CoFe_2O_4$/RGO-$CoFe_2O_4$) dispersed in 250 mL of 10 ppm 4-CP solution. The reaction mixture was stirred continuously using magnetic stirrer for entire time span of the experiment. During photochemical reaction process, a 5 mL aliquot sample were collected from the reaction suspension at definite time intervals and was subjected to centrifugation followed by filtration (through 0.4 μm millopore) to remove the catalyst particles for spectrophotometric analysis. Prior to irradiation, the reaction mixture was stirred for 30 min to ensure the establishment of adsorption/ desorption equilibrium (Fig.S2-S4). A plot of absorbance values against known concentration of 4-CP is plotted and this standard calibration curve is used for finding the unknown concentration. The extent of adsorption was calculated from the equation; $Q = (C_0 – C)V / W$, where Q is the extent of adsorption, C_0 and C are the concentrations (mg/L) before and after adsorption, V is the volume (L) of the reaction mixture and W is the amount of catalyst used (g). The unit of Q is mg g^{-1}. The residual concentration of 4-CP was determined by UV-vis spectrophotometer (Table. S5).

3. RESULTS and DISCUSSION

3.1. PXRD studies

The PXRD pattern of RGO, $CoFe_2O_4$ and RGO-$CoFe_2O_4$ nanocomposite are shown in the Figure.1. PXRD pattern of RGO shows 2θ peaks at 26° (002), 45° (004) and 55 ° (101) (JCPDS 41-1487). $CoFe_2O_4$ 2θ peaks appear at 30° (220), 36° (311), 37° (222), 43° (400), 55° (422), 57° (511), 63° (440), 71° (622) and 75° (533) (JCPDS 22-1086). RGO-$CoFe_2O_4$ nanocomposite shows 2θ peaks at 26.52° (002*), 30° (220), 36° (311), 43° (400), 45° (004*),

55°(422), 57° (511), 63° (440) and 75° (533). The hkl values are mentioned in the parenthesis. The PXRD results are consistent with the mentioned JCPDS standard pattern. The results obtained confirm the spinel crystal structure for $CoFe_2O_4$ and hexagonal structure for RGO. These native structures were well retained in the RGO-$CoFe_2O_4$ composite. The crystallite sizes were calculated by Debye-Scherer equation and were found to be 56.21 nm and 32.63 nm for $CoFe_2O_4$ and RGO-$CoFe_2O_4$ respectively. It is observed that the RGO in the RGO-$CoFe_2O_4$ nanocomposite was fully exfoliated and does not allow the crystal growth of $CoFe_2O_4$ nanoparticles between its interlayer sheets. The presence of RGO peaks along with the peaks corresponding to the $CoFe_2O_4$ in the PXRD pattern of RGO-$CoFe_2O_4$ nanocomposite catalyst indicate the absence of any structural change due to the exfoliation [37].

3.2. UV- visible spectroscopic studies

The optical characteristics of RGO, $CoFe_2O_4$ and RGO-$CoFe_2O_4$ were obtained from UV-visible absorption spectra as shown in Figure 2. The RGO exhibits a characteristic absorption peak around 250-300 nm corresponding to E_2 and B bands of $\pi-\pi^*$ transition of aromatic C=C bonds and the conjugation extends the absorption to the visible region. $CoFe_2O_4$ and RGO-$CoFe_2O_4$ shows continuous wide absorption in the wavelength range from UV to visible light region. The band gap values were determined from these spectra by converting the absolute absorption values to Kubelka-Munk function F (R_∞). The plot of Kubelka-Munk function $[F(R_\infty)hv]^{1/2}$ versus photon energy in electron volts (eV) gives the band gap energy values as shown in the inset of Figure.2 and the values were found to be 3.2 eV, 2.5 eV and 2.1eV for RGO, $CoFe_2O_4$ and RGO-$CoFe_2O_4$ respectively. The reduction of band gap of RGO-$CoFe_2O_4$ composite can be accounted in the following way: i) the major contribution is from the presence of RGO with its π electron system in the composite ; ii) the electrostatic binding between RGO and $CoFe_2O_4$ may bring about mixing up of energy levels of both the

materials; iii) delocalization of π electrons in the extensive RGO system; iv) charge transfer interaction between RGO and $CoFe_2O_4$ may shift the band edge positions in such a way that the band gap decreases. The broad absorption between 400-750 nm is attributed to the d-d transitions of Co^{2+} / Co^{3+} and Fe^{2+} / Fe^{3+}. Octahedral cobalt (II) compounds are expected to show an absorption peak between 400-600 nm and tetrahedral compounds show between 600-800 nm. The visible transitions are generally about an order of magnitude more intense and displaced to lower energy for tetrahedral compounds compared to octahedral systems. Because of small stability difference between octahedral and tetrahedral cobalt (II) compounds, both the types are usually expected to be present in equilibrium. Further iron (II) / (III) compounds are expected to show absorption between 400-1000 nm. But the actual observed spectra show continues absorption without any specific peaks due to the overlap of these absorption bands.

3.3. FTIR studies

The FTIR spectra of RGO, $CoFe_2O_4$ and RGO-$CoFe_2O_4$ are shown in Figure.3. The characteristic transmittance peak of spinel structure of $CoFe_2O_4$ was observed at 556 cm^{-1}. The absence of epoxy (1050 cm^{-1}), carboxylic C=O and OH (1720 and 1620 cm^{-1}) functional groups in the spectra confirms the complete reduction of GO to RGO. The presence of peak at 548 cm^{-1} in RGO-$CoFe_2O_4$ spectrum confirms the uniform distribution of cobalt ferrite spherical particles in the RGO layers. The observed small variation in the band position is due to the change in the chemical environment of Fe- O bond in the composite.

3.4. Raman spectroscopy

Raman spectroscopy is a powerful tool for investigating the electronic and phonon structure in pristine and coupled materials. The Raman spectra of RGO, $CoFe_2O_4$ and RGO-$CoFe_2O_4$ are shown in Figure.4. The GO is expected to show D and G bands at 1362 cm^{-1} and 1599 cm^{-1}. However these bands are slightly shifted on reduction of GO to RGO. The

observed band at 1360 cm^{-1} was due to the disordered sp^2 carbon and is termed as D band. The band at 1583 cm^{-1} was for well ordered RGO carbon (G band) [38]. The peaks observed at lower frequency values of 288 cm^{-1} and 477 cm^{-1} were due to the phonon modes of metal ions involved in octahedral groups (BO_6). These modes correspond to symmetric and antisymmetric bending modes of oxygen atom in metal-oxygen (M-O) bond at octahedral groups [39, 40]. The band at 700 cm^{-1} is of A_{1g} which arises due to the motions of oxygen atoms in tetrahedral structure of AO_4 type. There are many factors affecting the position and intensity of D and G bands such as defects, accompanied strain in coupling and doping etc., The observed Raman shifts in RGO-$CoFe_2O_4$ implies strong chemical interaction between RGO and $CoFe_2O_4$ nanocomposites. The intensities of all the RGO-$CoFe_2O_4$ peaks were significantly lower compared to $CoFe_2O_4$. This is due to the homogeneous wrapping of $CoFe_2O_4$ surface by RGO sheets.

3.5. Magnetic Property

Figure.5 shows the plot of extent of magnetization versus magnetic field strength for $CoFe_2O_4$ and RGO-$CoFe_2O_4$ samples at room temperature. The experimentally observed coercivity and saturation magnetization values from the hysteresis loop were found to be 1384 Oe and 56.71 emu/g for RGO–$CoFe_2O_4$ composite and 809 Oe and 14.08 emu/g for $CoFe_2O_4$. The above observed higher values for RGO-$CoFe_2O_4$ nanocomposite implies stronger extent of magnetization compared to $CoFe_2O_4$. Hence, RGO–$CoFe_2O_4$ composite particles can be more efficiently separated due its high magnetization values compared to $CoFe_2O_4$. The increase in the extent of saturation magnetization is directly related to the coupling of RGO with $CoFe_2O_4$, which affects the super exchange interaction.

3.6. BET surface measurements

The specific surface area and pore volume of $CoFe_2O_4$ and RGO−$CoFe_2O_4$ samples were determined by BET method (Figure 6a and b). The pore size distribution was obtained from

BJH method and was found to be 2.2-6.4 nm and 1.3-6 nm for RGO−$CoFe_2O_4$ and $CoFe_2O_4$ samples respectively. Specific surface area and total pore volume were found to be 25.18 m^2 g^{-1} and 0.022 ccg^{-1} for RGO−$CoFe_2O_4$ and 6.202 m^2 g^{-1} and 0.0031 ccg^{-1} for $CoFe_2O_4$ respectively. These values are relatively large for RGO−$CoFe_2O_4$ sample compared to pure $CoFe_2O_4$ due to the random packing of $CoFe_2O_4$ nanoparticles between RGO sheets. It is well-known from the literature that the reported specific surface area of RGO is as high as 2630 m^2 g^{-1} [41]. However, the specific surface area of the RGO−$CoFe_2O_4$ is much lower than the RGO due to the dispersion of $CoFe_2O_4$ nanoparticles on its surface.

3.7. FESEM images

The morphology of RGO, $CoFe_2O_4$ and RGO-$CoFe_2O_4$ were recorded by using FESEM. The morphology of RGO was found to be layered sheet like structure (Figure.7a). Morphology of $CoFe_2O_4$ was found to be spherical (Figure.7b). RGO-$CoFe_2O_4$ nanocomposite shows the distribution of $CoFe_2O_4$ spheres in between RGO layers. In addition the figure also depicts the aggregation of $CoFe_2O_4$ spheres which is because of the magnetic dipolar interaction among them. Average particle size of RGO-$CoFe_2O_4$ was found to be 28-67 nm. The composition of the samples was confirmed by EDS technique as shown in the Figure 8. The presence of Fe, Co, C, and O were confirmed. The atomic ratio of Fe to Co was found to be 2:1.

3.8. Photoluminescence spectra (PL)

The charge transfer and recombination processes of the photogenerated electron-hole pairs are studied by PL technique for RGO, $CoFe_2O_4$ and RGO-$CoFe_2O_4$ samples. RGO shows PL emission at 520 nm due to the recombination reactions occurring in the framework of extended conjugation. $CoFe_2O_4$ sample shows PL emissions at 270 and 480 nm as shown in the Figure.9. The valence band of $CoFe_2O_4$ is formed by oxygen 2p levels and the conduction band is from 3d levels of iron. The cobalt 3d levels are located much higher than

conduction band edge. The peak at 270 nm should be because of the recombination reactions involving cobalt 3d levels, whereas the peak at 480 nm is due to the recombination reactions taking place between the valence band and conduction band. The oxidation of Co (II) to Co (III) results in change from high to low spin and it takes place in two steps. The first step being rearrangement of electrons in low spin state and second step will be removal of e_g electron to generate Co (III). $Co^{2+}\left(t^5_{2g}eg^2\right) \rightarrow Co^{2+}\left(t^6_{2g}eg^1\right) \rightarrow Co^{3+}\left(t^6_{2g}eg^0\right)$. The PL emission of RGO-$CoFe_2O_4$ sample was observed between 650-800 nm. The peak which was observed at 270 nm for $CoFe_2O_4$ is completely diminished in the case of RGO-$CoFe_2O_4$. The only recombination reaction occurring in the RGO-$CoFe_2O_4$ composite is in the extended conjugation of RGO framework.

3.9 Photoelectrochemical studies

The transient photocurrent response was recorded upon excitation of pure RGO, $CoFe_2O_4$ and RGO-$CoFe_2O_4$ dispersion in aqueous solution of sodium sulphate electrolyte under UV- light (Figure10). The photocurrent response was reproducible during the repeated on/off cycles under UV light irradiation. The photocurrent of the RGO-$CoFe_2O_4$ sample (7.31 μA) was about 2 times higher than that of the $CoFe_2O_4$ sample (3.26 μA), and 4 times higher than the RGO sample (1.87 μA). This indicates enhanced separation efficiency of photogenerated electrons and holes as a result of the electronic interaction between $CoFe_2O_4$ nanoparticles and RGO sheets. The photogenerated charge transfer process is more efficient under the influence of applied electric field for RGO-$CoFe_2O_4$. This may be because of unique transport properties of photogenrated charge carriers which behave as mass less fermions in two-dimensional π-conjugation structure of RGO in the nanocomposite system [42].

3.9. Photocatalytic activities of RGO, $CoFe_2O_4$ and RGO-$CoFe_2O_4$

Photocatalytic activities of RGO, $CoFe_2O_4$, RGO−$CoFe_2O_4$ catalysts for the oxidation of 4-CP was explored under visible light illumination (Figure.11 and Table 1). 250 ml of 10 ppm 4-CP solution was completely degraded in 120 min in the presence of RGO−$CoFe_2O_4$, whereas 73% of degradation takes place with $CoFe_2O_4$ in 150 min. In the case of RGO, 50% of degradation takes place in 180 min. The significant enhancement in the photocatalytic activity of RGO-$CoFe_2O_4$ can be attributed to the remarkable synergistic effect between the photocatalyst $CoFe_2O_4$ and the extended conjugation of RGO samples. Efficient separation of photogenerated charge carriers takes place due to the presence of RGO. Such an enhancement in catalytic activity is due to the unique π-π stacking electronic structure of RGO and high migration efficiency of electrons in its framework.

For calculating the rate constant a plot of $\ln(C/C_o)$ versus time is plotted, where C_0 and C is the initial concentration and concentration at time t respectively. The rate constant k is calculated from the slopes of the fitted straight lines [43]. The experimental data obtained fit well with the pseudo first order reaction kinetics ($\ln(C/C_o) = -kt$).

3.10. Effect of PMS as an oxidant

The effect of electron scavenging species on the degradation mechanism was studied by taking PMS, which acts as an oxidant. The concentration of PMS was varied from 20-80 ppm while keeping the dosage of RGO-$CoFe_2O_4$ as constant and the obtained results are shown in Figure.12 and Table 2. The degradation reaction rate increased sequentially up to 60 ppm. The degradation rate decreased with further increase in the PMS concentration. At higher PMS concentration excess $SO_4^{\bullet -}$ and •OH free radicals are formed which may recombine in the bulk of the solution by geminate recombination [44]. Further, increasing the PMS concentration at constant catalyst dosage, excessive HSO_5^- ions may scavenge $SO_4^{-\bullet}$ and •OH free radicals in the solution leading to the formation of less reactive $SO_5^{-\bullet}$ radical as

shown in equation 1. Therefore, the increment of degradation rate with oxidant dosage is linear up to optimum concentration, further increase in the dosage leads to deviation from the linearity.

$$HSO_5^- + SO_4^{-\bullet}/{}^{\bullet}OH \rightarrow SO_5^{-\bullet} + SO_4^{2-} + H^+/OH^- \quad (1)$$

The control experiments were performed for RGO and $CoFe_2O_4$ photocatalysts by taking 60 ppm PMS solution. 20% decomposition takes place with RGO in 150 min and 45% degradation takes place with $CoFe_2O_4$ in 120 min.

3.11. Effect of RGO-$CoFe_2O_4$ catalyst dosage

Keeping the oxidant dosage constant as 60 ppm, the dosage of RGO-$CoFe_2O_4$ was varied from 0.1-0.25 g. Generally, it is expected that as the concentration of the catalyst is increased the rate of the degradation should also increase due to the increase in the number of active sites to generate more functional free radicals. The enhancement in the degradation rate was observed up to 0.2 g. Further increase in the catalyst dosage to 0.25 g the rate of the reaction was suppressed to certain extent (Figure.13 and Table 3). The adverse effect observed for high amounts of catalyst can also be endorsed to the difficulty of photons reaching each catalyst particle in the aqueous reaction suspension. Further the electron scavenging effect by the free radicals generated from the catalyst particles can dominate at higher concentrations as shown in the following equations:

$$CoFe_2O_4\text{-}RGO\,(e) + SO_4^{-\bullet}/{}^{\bullet}OH \rightarrow CoFe_2O_4\text{-}RGO\,(h^+) + SO_4^{2-}/{}^{-}OH \quad (2)$$

$$Co^{2+} + SO_4^{-\bullet}/{}^{\bullet}OH \rightarrow Co^{3+} + SO_4^{2-}/{}^{-}OH \quad (3)$$

$$Fe^{3+} + SO_4^{\cdot-}/{}^{\cdot}OH \rightarrow FeSO_4/[Fe(OH)]^{2+} \quad (4)$$

3.12. Effect of initial concentration of substrate 4-CP

The reaction conditions were further standardised for the concentration of the substrate 4-CP by maintaining the constant concentration of RGO-$CoFe_2O_4$ catalyst (0.2 g) and PMS (60 ppm). Initial 4-CP concentration was varied from 10-40 ppm by maintaining the optimum

reaction parameters. The maximum concentration of 4-CP which can be efficiently degraded for the reaction conditions mentioned above has been found to be 30 ppm and the degradation takes place within 60min (Figure 14 and Table 4). With further increase in the concentration of 4-CP to 40 ppm the rate of degradation decreased. The number of active sites on the catalyst surface and reactive free radicals like $SO_4^{-\bullet}$ and •OH were quite sufficient for the degradation of 30 ppm concentration, but were found to be less for 40 ppm 4-CP concentration.

3.13. Discussion of RGO-$CoFe_2O_4$ photocatalytic reaction mechanism

Equation 5 shows the electron-hole pair generation in the RGO-$CoFe_2O_4$ composite under solar light illumination and the intramolecular charge transfer is depicted. The electrons moves into the RGO framework and the holes moves towards the catalyst- solution interface. More clearly the photogenerated electrons can migrate from the conduction band of $CoFe_2O_4$ to RGO extended framework within the nanocomposite and holes can migrate to the solution interface. The photogenerated electrons from RGO framework are easily trapped by the molecular oxygen to generate super oxide radical. Alternatively conduction band electrons can even be trapped by oxygen molecules directly. The hole at the interface can react with OH^-/H_2O to produce ·OH free radicals as shown in the equation 5-7.

$$\text{RGO-CoFe}_2\text{O}_4\text{ /Interface} \xrightarrow{h\nu} \text{RGO-CoFe}_2\text{O}_4\text{/Interface} \quad (5)$$

(e⁻ and h+ denote the electron and hole transfer)

$$RGO(e^-) - CoFe_2O_4\,(h^+) + O_2 \rightarrow RGO - CoFe_2O_4\,(h^+) + O_2^{\bullet-} \quad (6)$$

$$RGO - CoFe_2O_4\,(h^+) + OH^- / H_2O \rightarrow RGO - CoFe_2O_4 + {}^{\bullet}OH \quad (7)$$

$$RGO(e^-) - CoFe_2O_4\,(h^+) + HSO_5^- \rightarrow RGO - CoFe_2O_4 + {}^{\bullet}OH + SO_4^{\bullet-} \quad (8)$$

$$SO_4^{\bullet-} + H_2O \rightarrow HSO_4^- + {}^{\bullet}OH \quad (9)$$

$$Co^{2+} + HSO_5^- \rightarrow Co^{3+} + SO_4^{\bullet-} + {}^{-}OH \quad (10)$$

$$Fe^{3+} + e^{-} \rightarrow Fe^{2+} \quad (11)$$

$$Fe^{2+} + HSO_5^{-} \rightarrow Fe^{3+} + SO_4^{-\bullet} + OH^{-} \quad (12)$$

$$Fe^{3+} + HSO_5^{-} \rightarrow Fe^{2+} + SO_4^{2-} + OH^{-} \quad (13)$$

Various reaction mechanism/ pathways are involved in the degradation reaction mechanism: (i) the reaction rate was increased in the presence of PMS (H-O-O-SO_3) which acts as an oxidant (Eq. 8-9). PMS possess unsymmetrical structure, the SO_3 group in it can attract electrons and this end of O-O bond is negatively charged and hydrogen side is positively charged. The presence of PMS in a photocatalytic reaction is beneficial especially due to its unsymmetrical structure and dipolar nature of the molecule which posses lower unoccupied molecular orbital (LUMO) energy levels. The PMS molecule with unoccupied LUMO energy levels can readily accommodate photogenerated electrons more efficiently and shows better oxidising reactions; (ii) Co^{2+} ion in RGO-$CoFe_2O_4$ composite can easily bond with oxygen molecule by giving an electron. The resultant products can be Co^{3+} ion and super oxide radical. This activated super oxide radical can oxidise the organic substrate molecule. Simultaneously the reduction reaction involving super oxide radical can lead to the formation of H_2O_2. Both oxidation and reduction mechanisms are beneficial for the catalytic degradation reaction; (iii) transition metal ions are well known to attain multiple oxidation states. Cobalt and iron can be either in +2 or +3 oxidation state. The molecular formula of cobalt ferrite can be represented in two different ways: a) $Co[Fe_2]O_4$ in which case Fe^{3+} ions are present in the octahedral interstices, b) Fe^{2+} $[Co^{3+}$ $Fe^{3+}]O_4$, in this case half of the iron ions are in +2 oxidation state and remaining in +3 oxidation state. Cobalt is also present in +3 oxidation state. Further Fe^{2+} ions can occupy tetrahedral interstices and Co^{3+} ions are in octahedral interstices along with other half of Fe^{3+} ions. In the first case the preferential adopted structure can be spinel and in the second case the adopted structure is inverse spinel. The electron detrapping/trapping by either Co^{2+} ions or by Fe^{3+} ions (as shown in equations

10-13) will result in either spinel or inverse spinel structure. The transformation between the two structures may continuously take place during the photochemical reaction; (iv) Further iron can exist in +3 stable oxidation state having half filled $3d^5$ electronic configuration and cobalt can exist in +2 stable oxidation state corresponding to the electronic configuration of $3d^7$. The photogenerated electron trapped by either Fe^{3+} or by Co^{2+} ions changes this stable electronic configuration and the ions will spontaneously attain the stable state by either trapping/detrapping the electron during the photochemical reactions; (v) the recombination process occurring at 270 nm for $CoFe_2O_4$ is extensively quenched in RGO-$CoFe_2O_4$ due to the extended π -π conjugated framework as described in the PL technique; (vi) The higher magnitude of observed photocurrent for RGO-$CoFe_2O_4$ composite further substantiates the fact that efficient charge carrier separation takes place. The magnitude of photocurrent remains constant for several on and off cycles which exhibits good reproducibility. The magnitude of the photocurrent generated is two and four times higher than its counterparts due to the contribution of migrated electrons in RGO framework and also from the electrons generated in the conduction band of RGO-$CoFe_2O_4$ composite.

3.14. Reusability of the RGO-$CoFe_2O_4$ catalyst

The results of three consecutive experiments performed are given in Figure.15 and Table.5 The duration for completing the degradation reaction for first experiment was 120 min. At the end of the each experiment the catalyst was separated and then washed thrice with deionized water. The extent of degradation was found to be 80% and 65% for second and third repetitive cycles for the same time period of 120 min. The catalytic activity was retained for consecutive cycles and these findings show that the RGO-$CoFe_2O_4$ catalyst is stable, recoverable, and reusable.

4. Conclusion

The PXRD results of RGO-$CoFe_2O_4$ confirm the spinel structure and EDS results confirms the composition. The UV-visible absorption spectroscopic technique shows continuous absorption in visible region due to the overlap of many absorption bands and confirms the band gap to be 2.1 eV. FTIR spectrum confirms the spinel structure of $CoFe_2O_4$ and RGO-$CoFe_2O_4$. The observed Raman shifts for RGO-$CoFe_2O_4$ implies the strong chemical interaction between RGO and $CoFe_2O_4$. The higher saturation magnetization value of RGO-$CoFe_2O_4$ shows that these catalyst particles can also be separated efficiently by magnetization method. Lower PL intensity for RGO-$CoFe_2O_4$ implies lower recombination rate. Photocurrent measurement shows the efficient photogenerated charge carrier separation for RGO-$CoFe_2O_4$ and the catalyst can be used efficiently in an electrochemical system for energy and environmental applications. The photogenerated electron trapped by either Fe^{3+} or by Co^{2+} ions changes the stable electronic configuration and the ions will spontaneously attain the stable state by either trapping/detrapping the electron during the photochemical reactions.

Acknowledgements

Authors acknowledge the financial assistance from University Grants Commission (UGC) and Department of Science and Technology (DST), Government of India.

References.

[1] X. Y. Zhang, H. P Li, X. L Cui, Y. H Lin, Graphene/TiO_2 nanocoposites : synthesis , characterization and application in hydrogen evolution from water photocatalytic splitting, J. Mater. Chem. 20 (2010) 2801-2806.

[2] W. Low, V. Boonamnuayvitaya, A study of photocatalytic graphene–TiO_2 synthesis via peroxotitanic acid refluxed sol, Materials Research Bulletin. 48 (2013) 2809-2816.

[3] Y. R. Smith, A. Kar, V. R. Subramanian, Investigation of physicochemical parameters that influence photocatalytic degradation of methyl orange over TiO_2 nanotubes, Ind. Eng. Chem. Res. 48 (2009) 10268– 10276.

[4] Y. M. Li, X. J Lv, J. Lu, J. Li, Preparation of SnO_2- nanocrystal/graphene-nanosheets composites and their lithium storage ability, J. Phys. Chem. C. 114 (2010) 21770−21774

[5] M. Fujihira, Y. Satoh, T. Osa, Heterogeneous photocatalytic oxidation of aromatic compounds on TiO2. Nature. 293 (1981) 206−208.

[6] T. G. Xu, L. W. Zhang, H. Y. Cheng, Y. F. Zhu, Significantly enhanced photocatalytic performance of ZnO via graphene hybridization and the mechanism study, Appl. Catal. B. 101(2011) 382−387.

[7] C. Chen, W. Cai, M. Long, B. Zhou, Y. Wu, D.Wu, Y. Feng, Synthesis of visible-light responsive graphene oxide/TiO_2 composites with p/n heterojunction, ACS Nano. 4 (2010) 6425−6432.

[8] K. Woan, G. Pyrgiotakis, W. Sigmund, Photocatalytic carbonnanotube-TiO_2 composites, Adv. Mater. 21 (2009) 2233–2239.

[9] O. Rahman, S. C. Mohapatra, S. Ahmad, Fe_3O_4 inverse spinal super paramagnetic nanoparticles, Materials Chemistry and Physics. 132 (2012) 196– 202.

[10] Y. Jiang, Y. Wu, B. Xie, Y. Xie, Y. Qian, Moderate temperature synthesis of nanocrystalline Co_3O_4 via gel hydrothermal oxidation, Mater. Chem. Phys. 74 (2002) 234–237.

[11] X. Lou, J. Han, W. Chu, X. Wang, Q. Cheng, Synthesis and photocatalytic property of Co_3O_4 nanorods Synthesis and photocatalytic property of Co_3O_4 nanorods, Materials Science and Engineering: B. 137 (2007) 268–271

[12] B. H. Li, J. Cao, M. Shao, J. H. Qu ,Warner, Synthesis of Graphene@Fe_3O_4@C Core-Shell Nanosheets for High-Performance Lithium Ion Batteries, J. Mater. Chem. 21 (2011) 5069-5075.

[13] X. Chen, J. Chen, X. Qiao, D. Wang, X. Cai, Performance of nano Co_3O_4/peroxymonosulfate system: Kinetics and mechanism study using Acid Orange 7 as a model compound, Appl. Catal. B: Environ. 80 (2008) 116-121.

[14] Z. Ji, X. Shen, G. Zhu, H. Zhou, A.Yuan, Reduced graphene oxide/nickel nanocomposites: Facile synthesis, magnetic and catalytic properties, J. Mater. Chem. 2012, 22 (2012) 3471-3477.

[15] K. H. Chan, W. Chu, Degradation of atrazine by cobalt mediated activation of peroxymonosulfate: Different cobalt counter anions in homogenous process and cobalt oxide catalysts in photolytic heterogeneous process, Water Res. 43 (2009) 2513-2521.

[16] L. Ai, H. Huang, Z.Chen, X. Wei, J. Jiang, Activated carbon/$CoFe_2O_4$ composites: Facile synthesis, magnetic performance and their potential application for the removal of malachite green from water, Chem. Eng. J. 156 (2010) 243-249.

[17] X. Shu, J. He, D.Chen, Visible-light-induced photocatalyst based on nickel titanate nanoparticles, Ind. Eng. Chem. Res. 47 (2008) 4750−4753.

[18] P. X. Lian, H. Zhu, Z. XiangLi, W. Yang, H. Wang, Graphene Materilas : Fundamentals and emerging applications, Electrochim. Acta. 56 (2010) 834-840.

[19] V. K. Gupta, P. J. M. Carrott, Ribeiro Carrott, M. M. L. Suhas, Low-cost adsorbents: Growing approach to wastewater treatment-a review, Crit. Rev. Environ. Sci. Technol. 39 (2009) 783−842.

[20] A. B. Kashuba, Conductivity of deflectless gapahene, Phys. Rev. B. 78 (2008) 085415.

[21] C. X. Guo, H. B. Yang, Z. M. Sheng, Z. S. Lu, Q. L. Song, C. M. Li, Layered garphene/quantum dots for photovoltaic devices, Angew. Chem., Int. Ed. 49 (2010) 3014.

[22] S. R. Kim, M. K. Parvez, M. Chhowalla, UV-reduction of graphene oxide and its application as an interfacial layer to reduce the back-transport reactions in dye-sensitized solar cells Chem. Phys. Lett. 483 (2009)124-127.

[23] H. Zhang, , X. Lv Y. Li, Y.Wang, J. Li, P25-graphene composite as a high performance photocatalyst, ACS Nano. 4 (2010) 380−386.

[24] P.V. Kamat, Graphene-based nanoarchitectures, Anchoring semiconductor and metal nanoparticles on a two-dimensional carbon support, J. Phys. Chem. Lett. 1 (2010) 520–527.

[25] S. Shylesh, V. Schunemann, W. R. Thiel, Magnetically separable nanocatalysts: Bridges between homogeneous and heterogeneous catalysis, Angew. Chem., Int. Ed. 49 (2010) 3428−3459.

[26] S. Sun, H. Zeng, D. B. Robinson, S. P. Raoux, M. Rice, S.X. Wang, G. Li, Monodisperse MFe2O4 (M = Fe, Co, Mn) nanoparticles, J. Am. Chem. Soc. 126 (2004) 273−279.

[27] H. Deng, X. Li, Q. Peng, X.Wang, J. Chen, Y. Li, Monodisperse magnetic single crystal ferrite microspheres, Angew. Chem., Int. Ed. 44 (2005) 2782−2785.

[28] E. Casbeer, V. K. Sharma, X. Z. Li, Synthesis and photocatalytic activity of ferrite under visible light: A review, Sep. Purif. Technol. 87 (2012) 1−14.

[29] P.Xiong, Y.Fu, L.Wang, X. Wang, Multi-walled carbon nanotubes supported nickel ferrite: A magnetically recyclable photocatalyst with high photocatalytic activity on degradation of phenols, Chem. Eng. J. 195−196 (2012) 149−157.

[30] X. Chen, Q. Zhao, Li. Xinyong, D. Wang, Enhanced photocatalytic activity of degrading short chain chlorinated paraffins over reduced graphene oxide/CoFe2O4/Ag nanocomposite. J. Colloid Interface Sci. 479 (2016) 89-97.

[31] H.-Y. He, J. Lu. Highly photocatalytic activities of magnetically separable reduced graphene oxide-CoFe2O4 hybrid nanostructures in dye photodegradation, Sep. Purif. Technol.172 (2017) 374–381

[32] G. He, D. Jiajia, Z. Jianguo, Q. Hao, C. Haiqun, One-Step Ball-Milling Preparation of Highly Photocatalytic Active CoFe2O4−Reduced Graphene Oxide Heterojunctions For Organic Dye Removal Ind. Eng. Chem. Res. 54 (2015) 2862−2867

[33] M. Debabrata, C. Madhurya, G. Barun Kumar, J. Raj Kumar, P. Manoj Kumar, V. Sampat Raj, N. N. Ghosh, A simple 'in situ' co-precipitation method for the preparation of multifunctional CoFe2O4–reducedgraphene oxide nanocomposites: excellent microwave absorber and highly efficient magnetically separable recyclable photocatalyst for dye degradation RSC Adv. 6 (2016) 76759–76772

[34] Y. Wenzhu, H. Shuo, H. Cao, Solvothermal synthesis of magnetic CoFe2O4/rGO nanocomposites for highly efficient dye removal in wastewater, RSC Adv., 7 (2017) 4062–4069

[35] Z. X. Dafeng, Y.Gao, C. Su, H. Li, H. Li, H.Wenxian, One step combustion synthesis of CoFe2O4-graphene hybrid materials for photodegradation of methylene blue, Mater. Lett. 113 (2013) 179–181

[36] Y. S. Fu, X. Wang, Magnetically separable $ZnFe_2O_4$–Graphene catalyst and its high photocatalytic performance under visible light irradiation, Ind. Eng. Chem. Res. 50 (2011) 7210–7218.

[37] K. H. Chan, W.Chu, Degradation of atrazine by cobalt mediated activation of peroxymonosulfate: Different cobalt counteranions in homogenous process and cobalt oxide catalysts in photolytic heterogeneous process, Water Res. 43 (2009) 2513−2521.

[38] S. Stankovich, D. A. Dikin, R. D. Piner, K. A. Kohlhaas, A. Kleinhammes, Y. Jia, Y. Wu, S. T. Nguyen, R. S. Ruoff, Synthesis of graphene-based nanosheets via chemical reduction of exfoliatedgraphite oxide, Carbon. 45 (2007) 1558−1565.

[39] Z. W. Wang, D. Schiferl, Y. S. Zhao, S. C. O. Neill, High Pressure Raman Spectroscopy of Spinel-Type Ferrite ZnFe2O4, J. Phys. Chem. Solids. 64 (2003) 2517–2523.

[40] M. Maletin, E. G. Moshopoulou, A. G. Kontos, E Devlin, A. Delimitis, V. Zaspalis, L. Nalbandian, V. V. Srdic, Synthesis and Structural Characterization of In-Doped $ZnFe_2O_4$ Nanoparticles, J. Eur.Ceram. Soc. 27 (2007) 4391–4394.

[41] G. Ning, Z. Fan, G. Wang, J. Gao, W. Qian, F. Wei, Gramscale synthesis of nanomesh graphene with high surface area and its application in supercapacitor electrodes, Chem. Commun. 47 (2011) 5976−5978.

[42] K. K. Manga, Y. Zhou, Y. L. Yan, K. P. Loh, Multilayer Hybrid Films Consisting of Alternating Graphene and Titania Nanosheets with Ultrafast Electron Transfer and Photoconversion Properties, Adv. Funct. Mater. 19 (2009) 3638–3643.

[43] R. Kavitha, L. Gomathi Devi, Synergistic effect between carbon dopant in titania lattice and surface carbonaceous species for enhancing the visible light photocatalysis, J. Environ. Chemi. Eng. 2 (2014) 857–867

[44] L. Gomathi Devi, M. Srinivas, M.L. Aruna Kumari, Heterogeneous advanced photo-Fenton process using peroxymonosulfate and peroxydisulfate in presence of zero valent metallic iron: A comparative study with hydrogen peroxidephoto-Fenton process, J. Water Process Eng. 13 (2016) 117–126.

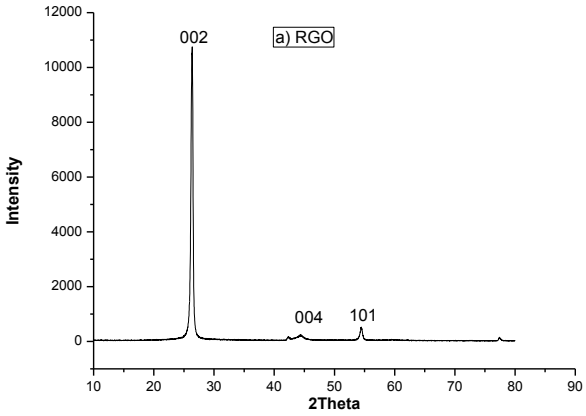

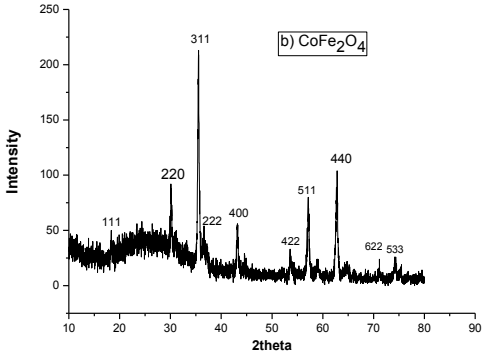

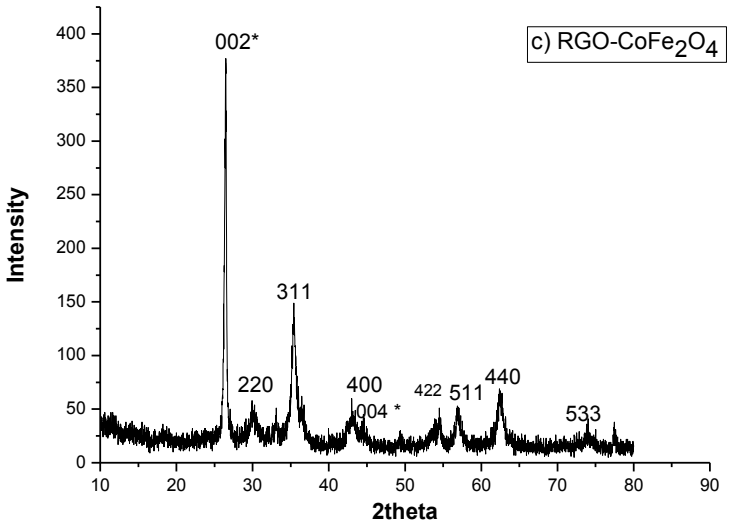

Figure.1. PXRD pattern of a) RGO b) $CoFe_2O_4$ c) RGO-$CoFe_2O_4$

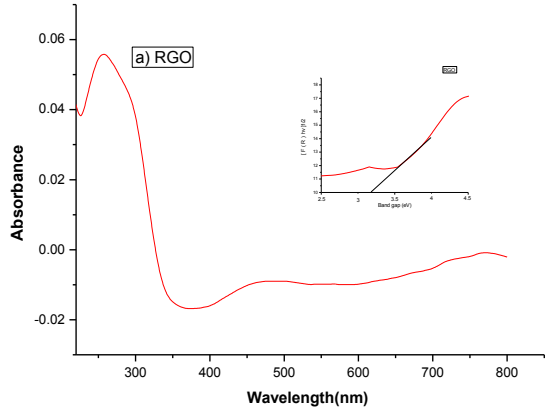

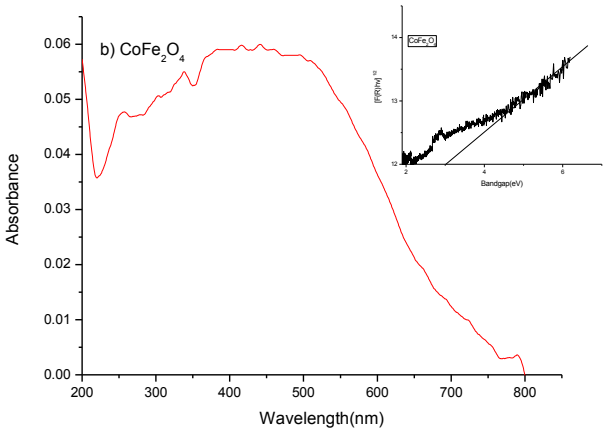

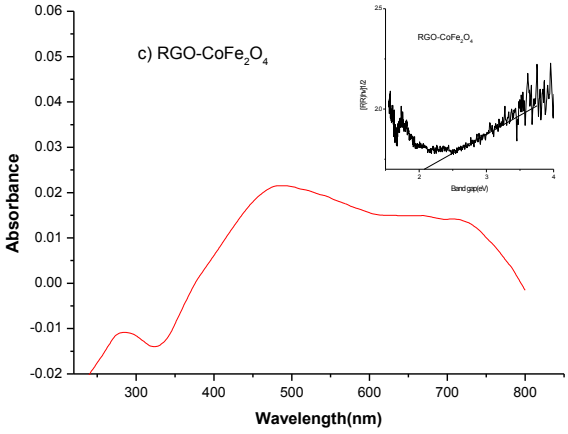

Figure.2. UV-Visible absorbance spectra of a) RGO b) $CoFe_2O_4$ c) RGO-$CoFe_2O_4$. The inset figure shows Kubelka-munk plots.

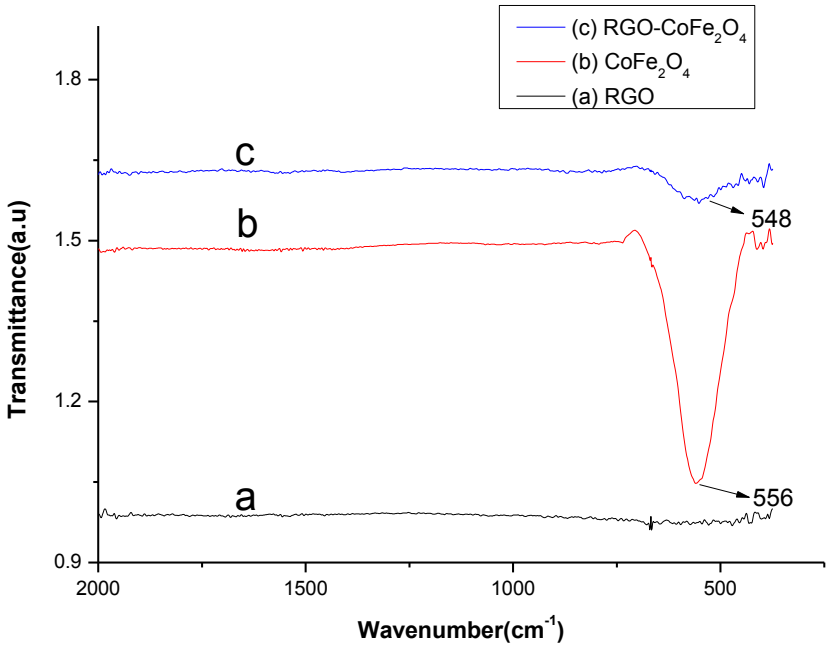

Figure.3. FTIR spectra of a) RGO b) $CoFe_2O_4$ c) RGO-$CoFe_2O_4$

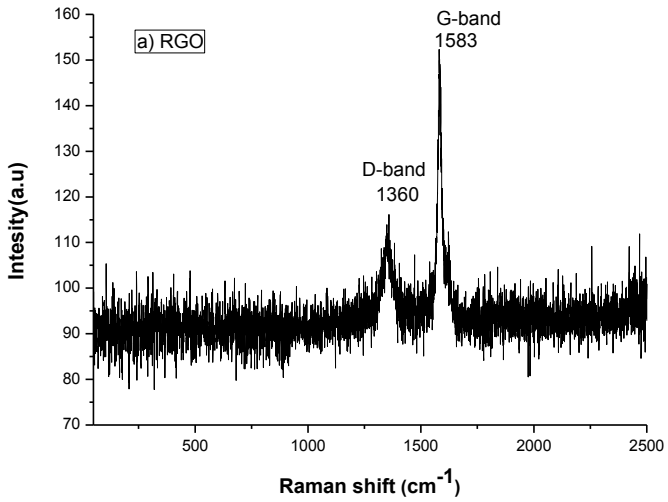

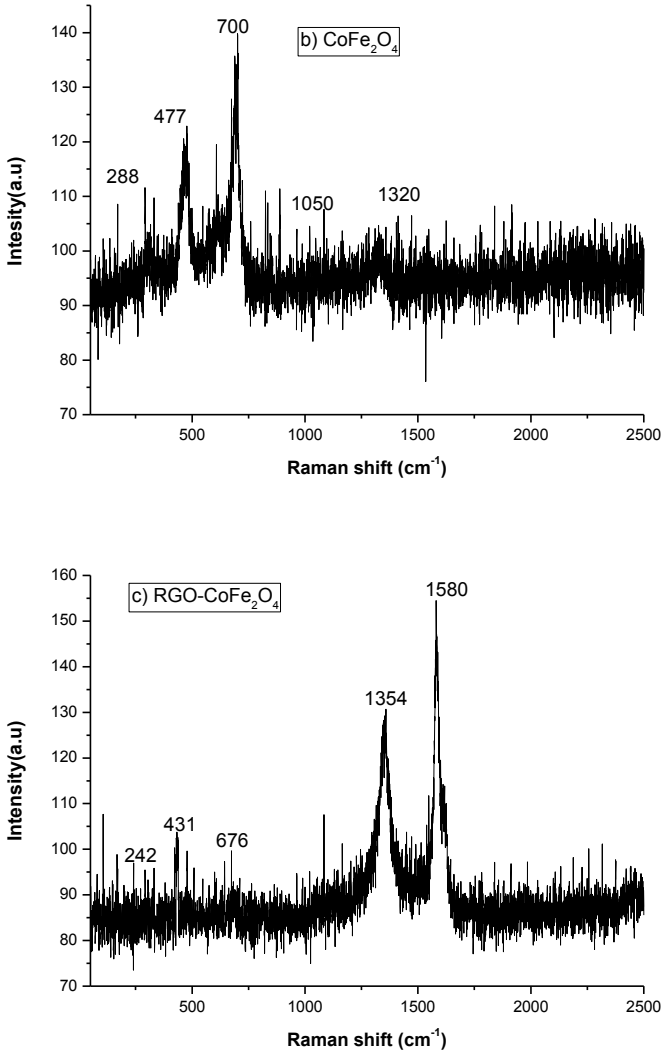

Figure.4. Raman spectra of a) RGO b) $CoFe_2O_4$ c) RGO-$CoFe_2O_4$

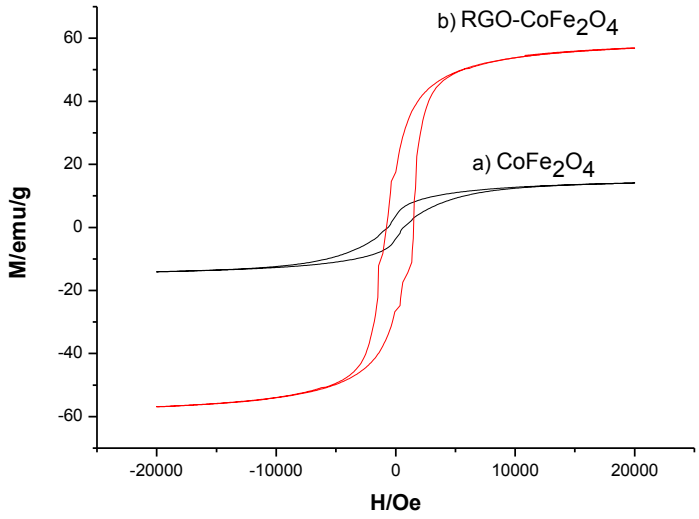

Figure.5. Magnetic hysteresis loops of a) $CoFe_2O_4$ and b) RGO-$CoFe_2O_4$

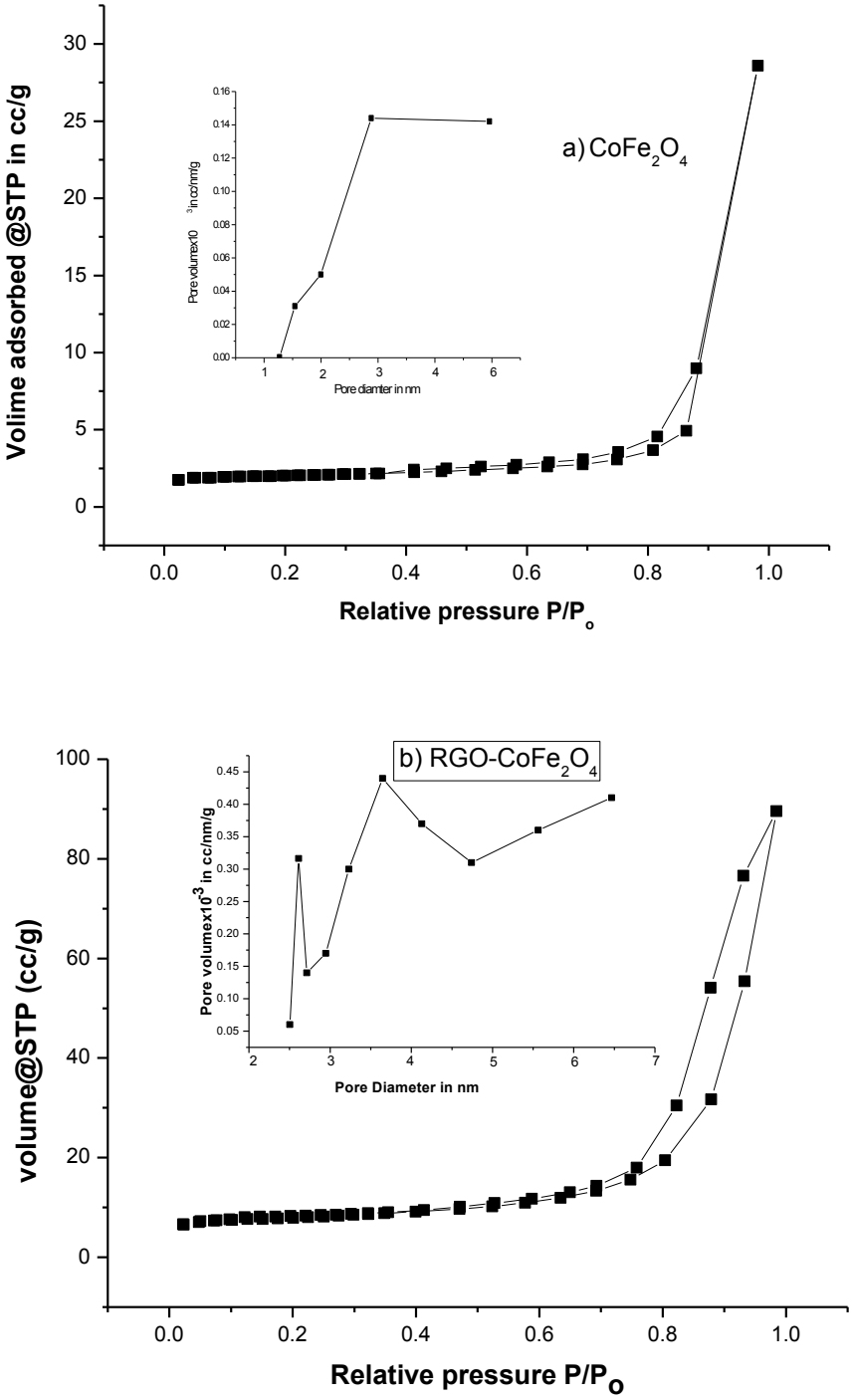

Figure.6. The N_2 adsorption–desorption isotherms of a) $CoFe_2O_4$ b) RGO-$CoFe_2O_4$. Inset figure shows BJH pore size distribution curve.

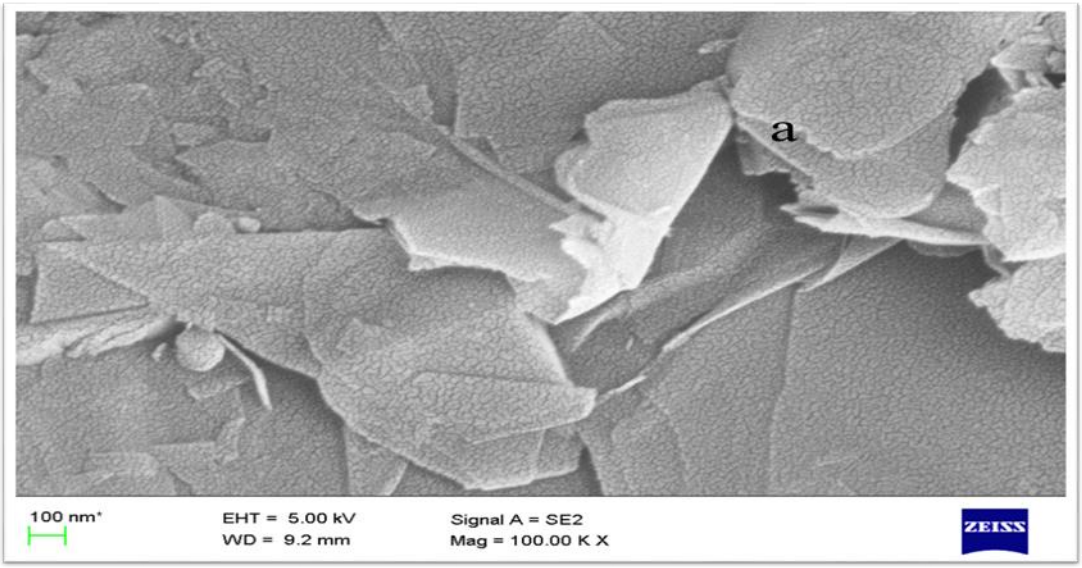

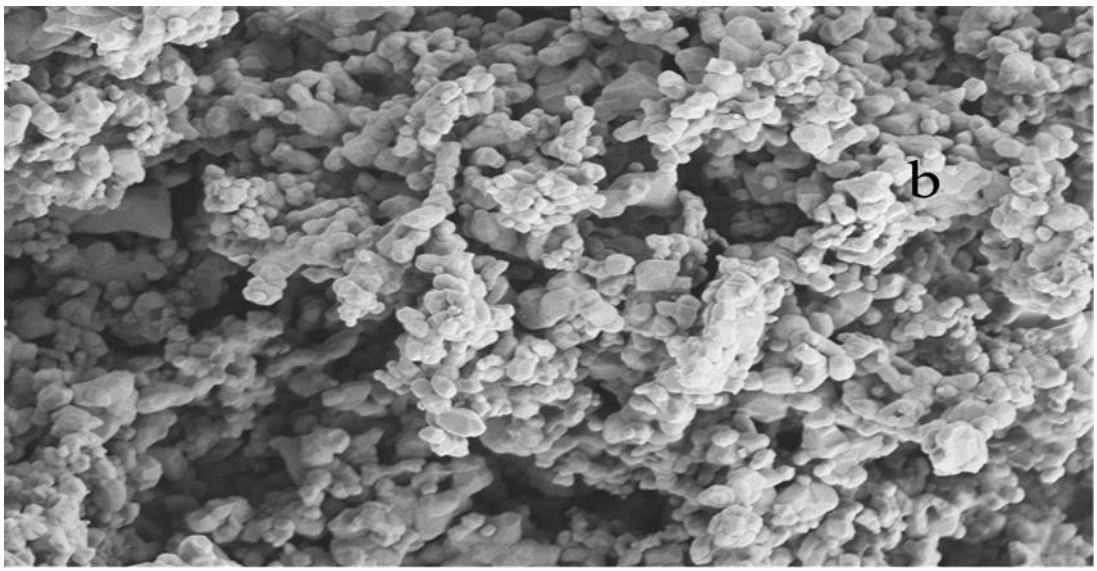

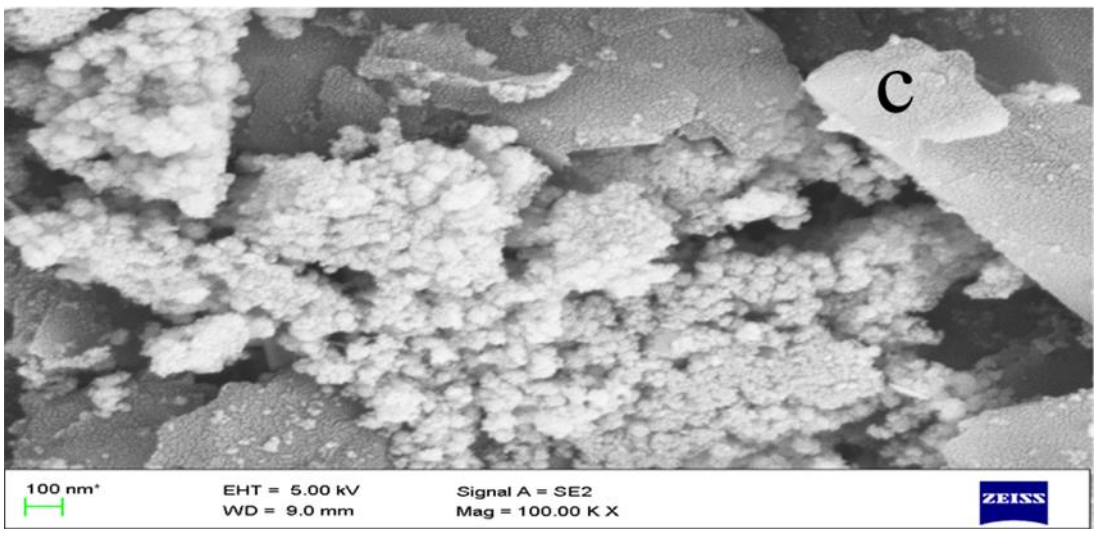

Figure.7. FESEM images of a) RGO b) $CoFe_2O_4$ c) RGO- $CoFe_2O_4$

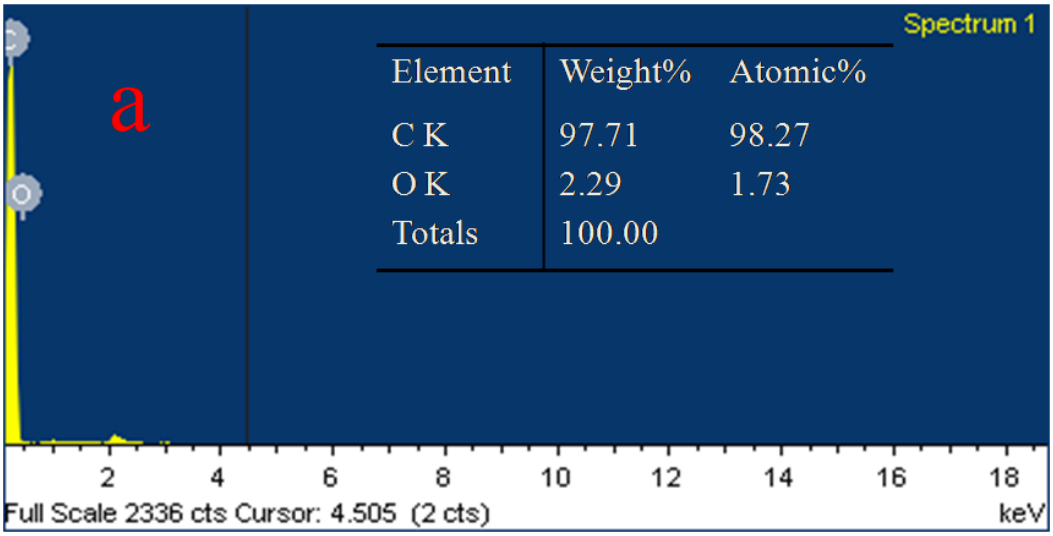

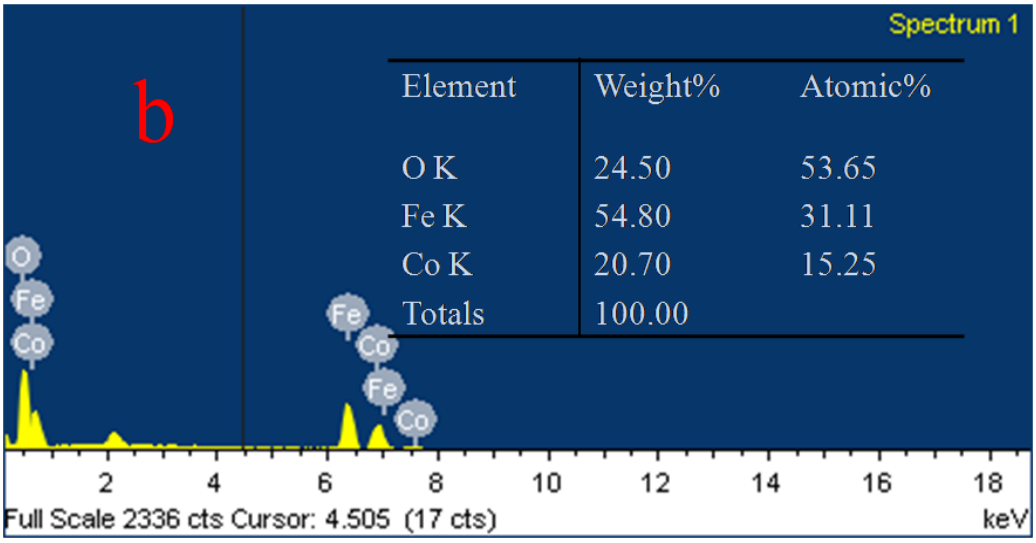

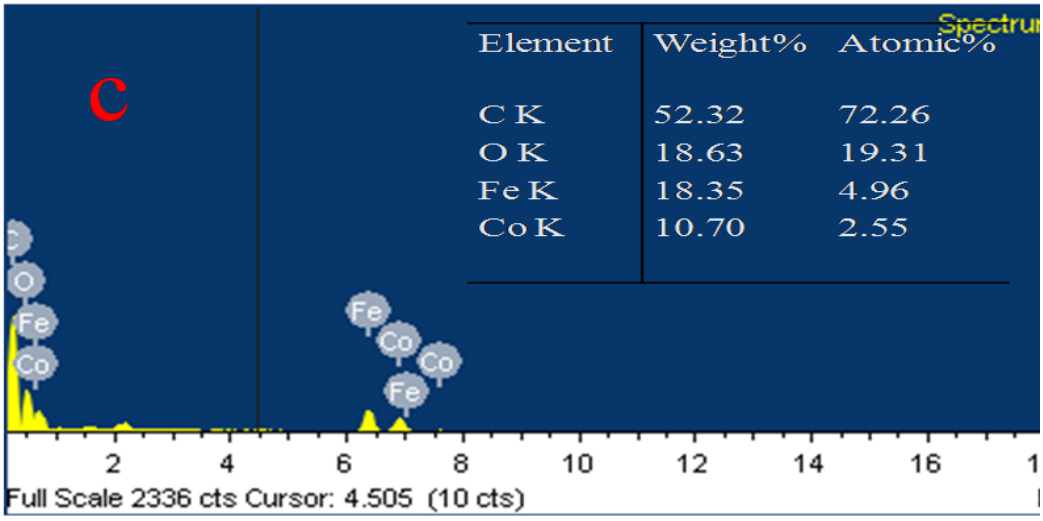

Figure.8. EDS of a) RGO b) $CoFe_2O_4$ c) RGO-$CoFe_2O_4$

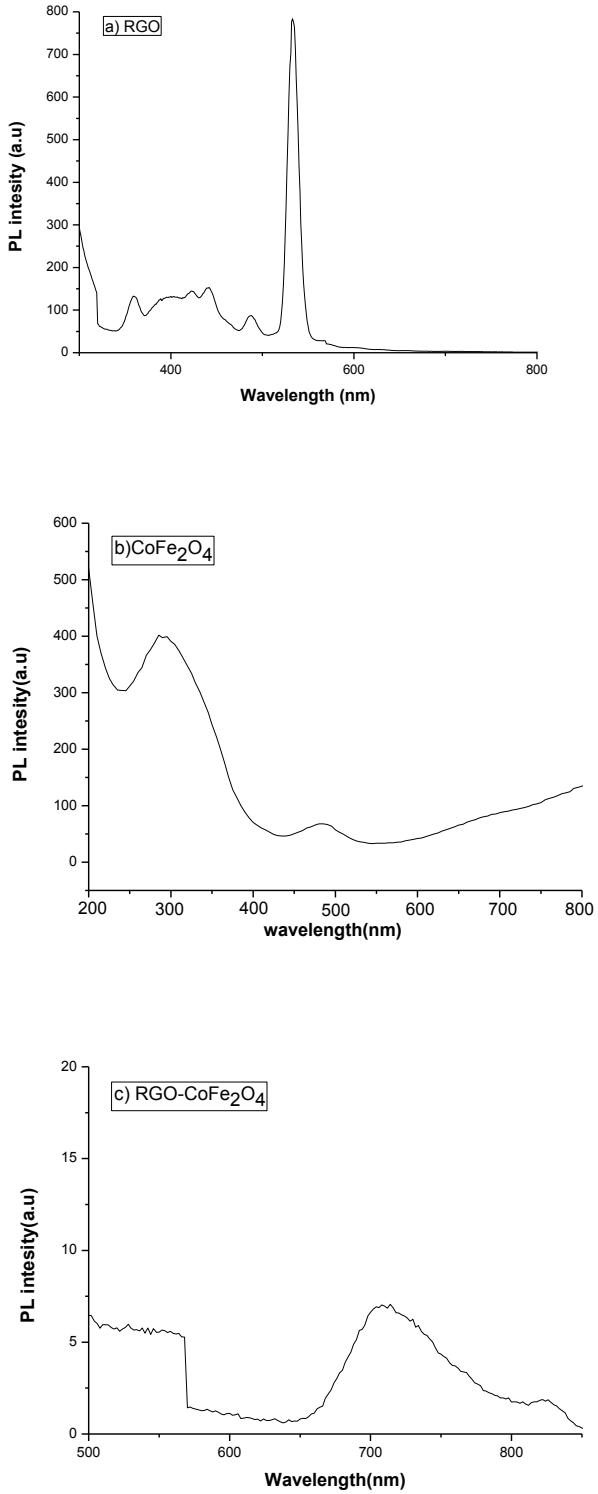

Figure.9. PL spectra of a) RGO b) $CoFe_2O_4$ c) RGO-$CoFe_2O_4$

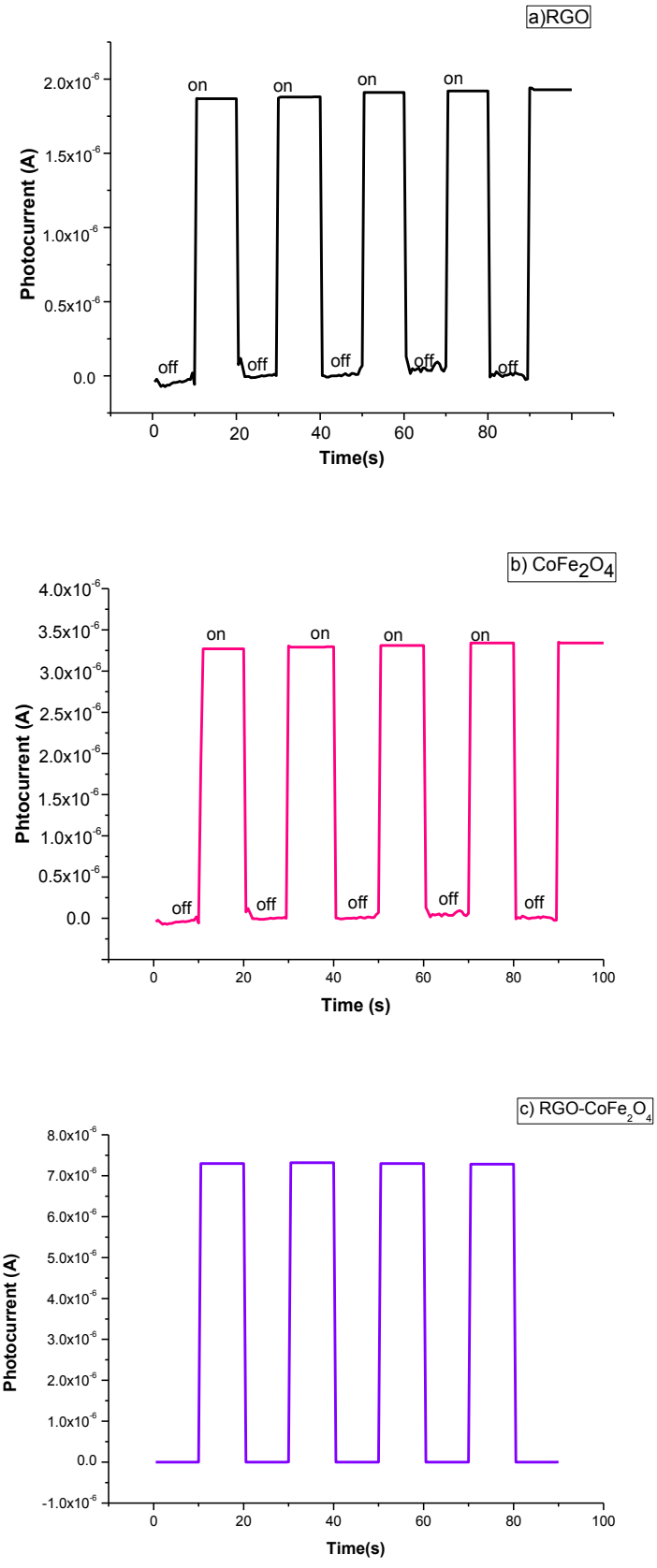

Figure.10. Transient photocurrent responses of a) RGO b) $CoFe_2O_4$ c) RGO-$CoFe_2O_4$

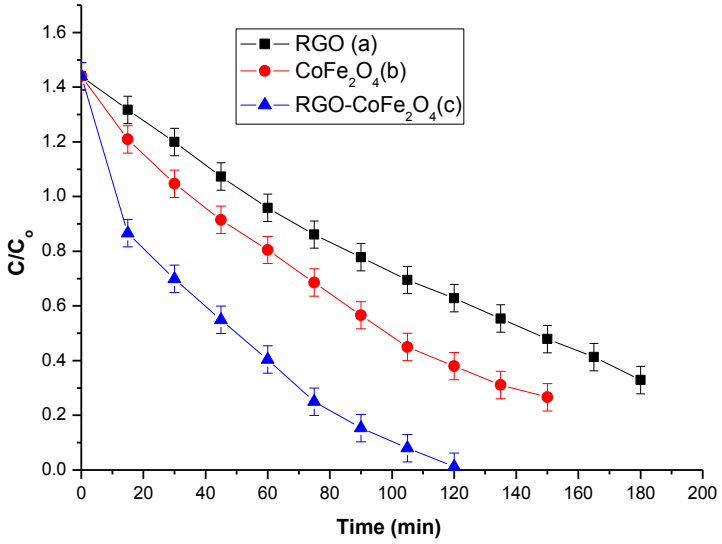

Figure.11: Plot of C/C_o vs. time in minutes for the degradation of 4-CP (10 ppm) along with 0.1 g of catalyst.

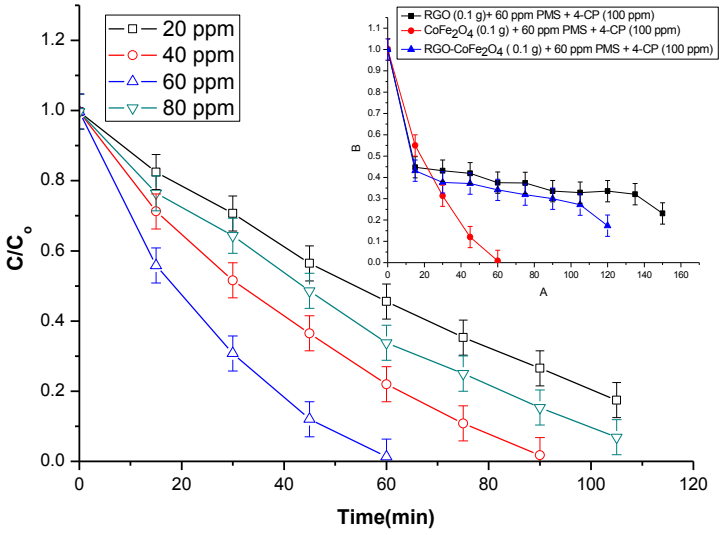

Figure.12: Plot of C/C_o vs. time in minutes for the degradation of 10 ppm 4-CP along with 0.1 g of catalyst at different PMS concentration. The inset shows the extent of 4-CP degradation with RGO, $CoFe_2O_4$ and RGO-$CoFe_2O_4$ photocatalysts along with 60 ppm PMS as oxidant.

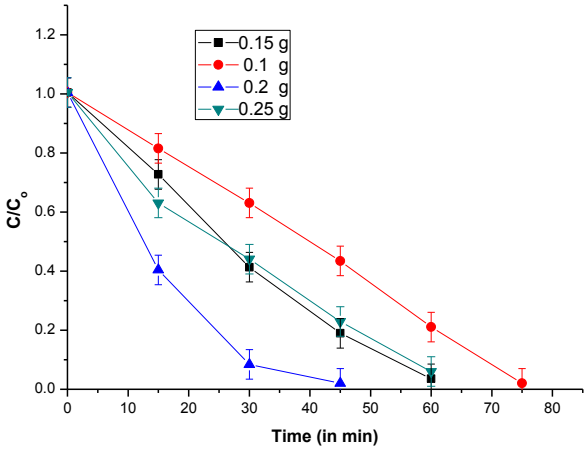

Figure 13: Plot of C/C_o vs. time in minutes for the degradation of 4-CP (10 ppm) along with 60 ppm PMS at different RGO-$CoFe_2O_4$ dosage

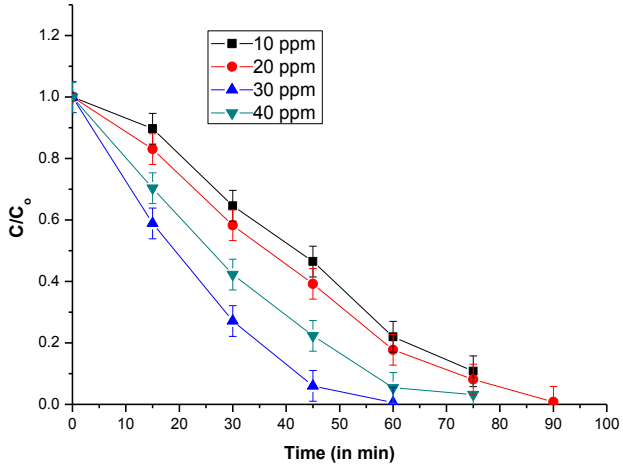

Figure14: Plot of C/C_o vs. time in minutes for the degradation of 4-CP along with PMS (60 ppm) and 0.2 g of RGO-$CoFe_2O_4$ at different 4-CP concentration

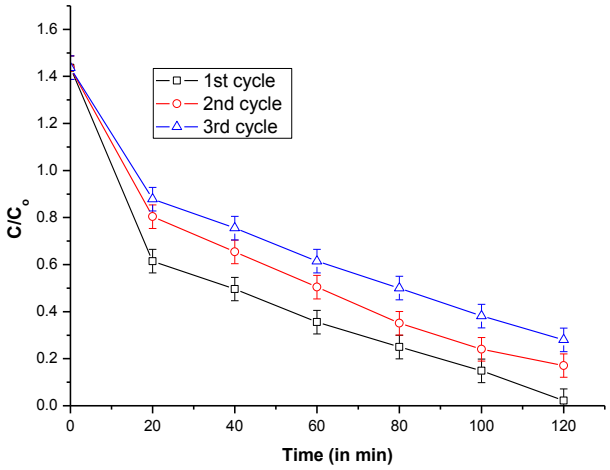

Figure.15: Reusability of RGO-$CoFe_2O_4$ (0.1 g) along with 250 ml of 4-CP (10 ppm) solution for three repeated cycles.

Tables

Photocatalyst	Rate constant x 10^{-2} min^{-1}	Degradation time (min)	Correlation coefficient (R^2)
RGO	0.7828	180	0.9930
$CoFe_2O_4$	1.1327	150	0.9852
RGO-$CoFe_2O_4$	3.3431	120	0.9462

Table.1. Rate constant and correlation coefficient values for the degradation of 4-CP along with degradation times (catalysts dosage = 0.1 g, 4-CP concentration = 10ppm)

PMS Concentration (ppm)	Rate constant x 10^{-2} min^{-1}	Degradation time (min)	Correlation coefficient (R^2)
20	1.605	105	0.9943
40	3.889	90	0.9828
60	6.910	60	0.9884
80	1.763	105	0.9677
60 + RGO	0.866	150	0.9758
60+ $CoFe_2O_4$	1.365	120	0.9907

Table.2. Degradation time, rate constant and correlation coefficient values for the degradation of 4-CP at different PMS concentration (catalysts dosage = 0.1 g RGO-$CoFe_2O_4$; 4-CP concentration = 10ppm)

RGO-$CoFe_2O_4$ dosage (g)	Rate constant x 10^{-2} min^{-1}	Degradation time (min)	Correlation coefficient (R^2)
0.1	2.9742	75	0.9388
0.15	4.8587	60	0.9929
0.2	8.5821	45	0.9871
0.25	4.4750	60	0.9995

Table.3. Degradation time and rate constant values for the degradation of 4-CP at different catalyst dosages (4-CP concentration = 10 ppm and PMS concentration = 60 ppm)

4-CP concentration (ppm)	Rate constant x 10^{-2} min^{-1}	Degradation time (min)	Correlation coefficient (R^2)
10	2.9424	75	0.9941
20	5.2491	90	0.9867
30	11.0337	60	0.9639
40	4.8308	75	0.9717

Table.4. Degradation time, rate constant and correlation coefficient values for the degradation of 4-CP at different concentrations (RGO-$CoFe_2O_4$= 0.2 g and PMS concentration = 60 ppm)

Cycles	Rate constant x 10^{-2} min^{-1}	Degradation time (min)	Correlation coefficient (R^2)
1 cycle	2.4253	120	0.8914
2 cycle	1.6854	120	0.9297
3cycle	1.2446	120	0.9387

Table.5. Degradation time, rate constant and correlation coefficient values for the degradation of 4-CP for three consecutive repeated cycles (RGO-$CoFe_2O_4$ = 0.1 g and 4-CP concentration = 10ppm)